npj | Quantum Materials

www.nature.com/npjquantmats

ARTICLE OPEN

# Field-induced resistance peak in a superconducting niobium thin film proximity coupled to a surface reconstructed $SrTiO_3$

Akhilesh Kr. Singh[1], Uddipta Kar[1,2], Matthew D. Redell[3], Tsung-Chi Wu[1], Wei-Hsiang Peng[1], Bipul Das[1], Satish Kumar[1], Wei-Cheng Lee[3]✉ and Wei-Li Lee[1]✉

Oxygen vacancy is known to play an important role for the physical properties in $SrTiO_3$(STO)-based systems. On the surface, rich structural reconstructions had been reported owing to the oxygen vacancies, giving rise to metallic surface states and unusual surface phonon modes. More recently, an intriguing phenomenon of a huge superconducting transition temperature enhancement was discovered in a monolayer FeSe on STO substrate, where the surface reconstructed STO (SR-STO) may play a role. In this work, SR-STO substrates were prepared via thermal annealing in ultra-high vacuum followed by low energy electron diffraction analyses on surface structures. Thin Nb films with different thicknesses (*d*) were then deposited on the SR-STO. The detailed studies of the magnetotransport and superconducting property in the Al(1 nm)/Nb(*d*)/SR-STO samples revealed a large positive magnetoresistance and a pronounced resistance peak near the onset of the resistive superconducting transition in the presence of an in-plane field. Remarkably, the amplitude of the resistance peak increases with increasing fields, reaching a value of nearly 57% of the normal state resistance at 9 T. Such resistance peaks were absent in the control samples of Al(1 nm)/Nb(*d*)/STO and Al(1 nm)/Nb(*d*)/$SiO_2$. Combining with DFT calculations for SR-STO, we attribute the resistance peak to the interface resistance from the proximity coupling of the superconducting niobium to the field-enhanced long-range magnetic order in SR-STO that arises from the spin-polarized in-gap states due to oxygen vacancies.

*npj Quantum Materials* (2020)5:45 ; https://doi.org/10.1038/s41535-020-0242-4

## INTRODUCTION

One intriguing factor governing the physical property in an oxide system is the oxygen content. In cuprates, extensive studies have demonstrated the effective tuning of the superconducting properties by simply varying the oxygen content in the parent compounds[1–3]. On the other hand, it is also known that oxygen vacancies in $SrTiO_3$ (STO) serve as electron donors[4], which turns the STO from a wide band-gap insulator into an unusual dilute superconductor[5]. As it turns out, the influence of the oxygen vacancies to STO can be multifold according to some recent investigations[6–8]. Microscopically, oxygen vacancies locally break the *d*-orbital symmetry of titanium ions, giving rise to unusual in-gap states and possible magnetism. Such in-gap states in oxygen-deficient STO have been observed in angle resolved photo-emission spectroscopy and scanning tunneling spectroscopy measurements[9,10]. More recently, a remarkable and nearly 10-fold enhancement of superconducting transition temperature was discovered in a monolayer of FeSe on STO[11], which motivates numerous investigations to reveal the intrinsic mechanism for such a huge $T_c$ enhancement[12,13]. Among various possibilities, oxygen vacancy and charge transfer from STO substrate are potential factors[14], and more experimental efforts are keenly required. In light of this quest, we study the influence of the superconducting property in thin niobium (Nb) films deposited on surface reconstructed STO (SR-STO) substrates. The SR-STO substrate can be prepared by annealing $TiO_2$-terminated STO in an ultra-high vacuum (UHV) environment, and the resulting oxygen vacancies cause structural reconstruction at the STO surface that can be identified by low energy electron diffraction (LEED) measurement and analysis. A striking field-induced resistance peak was uncovered at temperatures near the onset of the superconductivity in niobium, which is absent in zero field and also in control samples of niobium films deposited either on $SiO_2$/Si substrate or on $TiO_2$-terminated STO without any surface reconstruction. Surprisingly, the magnitude of resistance peak is more pronounced with in-plane fields and appears to grow with increasing field strength. The DFT calculations were carried out using oxygen vacancy structures obtained from the LEED analysis, where a unique spin-polarized in-gap states was found. The peak resistance phenomenon in Nb/SR-STO is likely resulting from the interplay between the superconducting Nb and the magnetism from the spin-polarized in-gap states of SR-STO.

## RESULTS

For more than ten $TiO_2$-terminated STO substrates we prepared, several annealing temperatures ranging from 800 °C to 900 °C were used with an annealing time of 4 h, and those substrates were then cooled down to room temperature for the LEED characterizations. The LEED pattern transformed from a simple cubic structure of major diffraction spots (Fig. 1a) into a much more complex pattern with additional secondary diffraction spots that come from the surface structural reconstruction effect. We also note that the diffraction spots become broader with different intensity after UHV annealing, indicating an increase in the surface roughness and also the inelastic scattering contribution to the LEED pattern. A rich variety of surface structure on STO after UHV annealing has been reported previously by many authors[15–17], where annealing temperature and duration are both crucial factors. For the following Al(1 nm)/Nb(*d*)/SR-STO sample

[1]Institute of Physics, Academia Sinica, Nankang, Taipei 11529, Taiwan. [2]Nano Science and Technology, Taiwan International Graduate Program, Academia Sinica and National Taiwan University, Nankang, Taiwan. [3]Department of Physics Applied Physics, and Astronomy, Binghamton University, Binghamton, NY 13902, USA. ✉email: wlee@binghamton.edu; wlee@phys.sinica.edu.tw

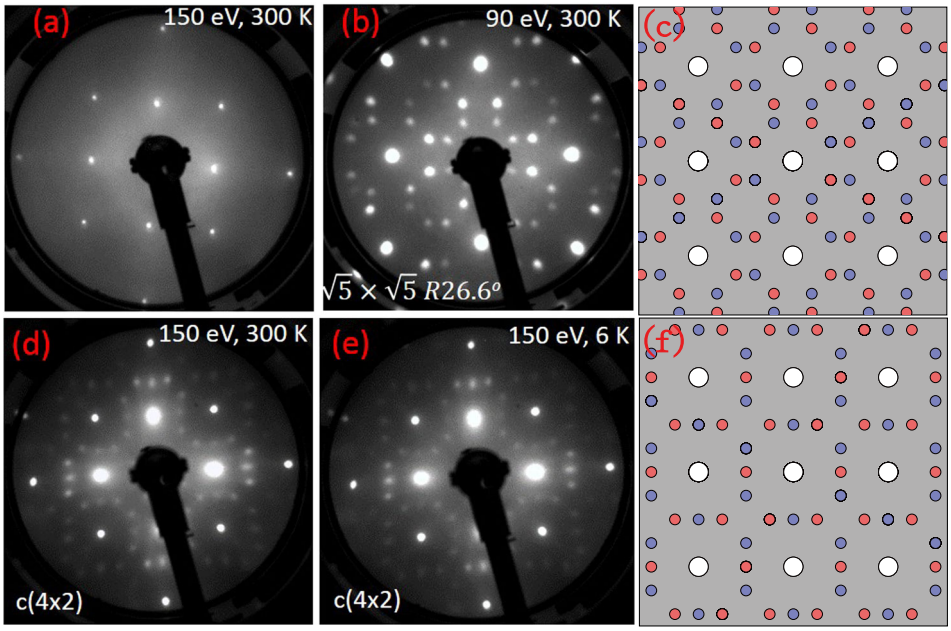


**Fig. 1 The surface structure of SR-STO.** The LEED patterns of $TiO_2$-terminated STO(100) substrates at room temperature: **a** no surface structural reconstruction. **b** $\sqrt{5} \times \sqrt{5}R26.6°$ surface structure after UHV annealing. **d** $c(4 \times 2)$ surface structure after UHV annealing. **c**, **f** are the simulated LEED patterns based on the $\sqrt{5} \times \sqrt{5}$ R26.6° and $c(4 \times 2)$ surface structures, respectively, showing excellent agreements with observed LEED patterns. The red and blue circles represent the secondary diffraction spots from different surface structure domains. Those surface structures after UHV annealing are stable after cooling down to lower temperatures. **e** shows the LEED pattern at 6 K, which is identical to that with $c(4 \times 2)$ surface structure at room temperature.

preparations, we chose to use the annealing temperature of 850 °C and annealing time of 4 h for the preparation of all SR-STO substrates. With this annealing condition, two distinct and reproducible surface structures can be identified from the LEED measurements. They are $\sqrt{5} \times \sqrt{5}$ R26.6° structure and c(4x2) structure, which are shown in Fig. 1b and d, respectively. The simulated LEED patterns using LEEDpat package[18] with $\sqrt{5} \times \sqrt{5}$ R26.6° and c(4 × 2) structures, shown in Fig. 1c and f, respectively, are in excellent agreements with the patterns we observed. The red and blue circles are secondary diffraction spots, deriving from different surface structure domains. We also note that those surface structures of SR-STO are stable down to lower temperatures. Fig. 1f is an example of the LEED pattern of c(4 × 2) structure measured with SR-STO at 6 K, showing negligible changes as compared to that at room temperature (Fig. 1d).

In order to study the influence of the proximity coupling between SR-STO and the superconducting Nb layer, control samples using different substrates of $SiO_2$/Si and STO were fabricated for comparison. The sample composition is illustrated in the lower inset cartoon of Fig. 2a. Figure 2a shows the temperature dependence of the sheet resistance $R_s$ for Al(1 nm)/Nb(10 nm)/Sub. with Sub. = STO, $SiO_2$/Si and SR-STO. The sheet resistance $R_s$ equals 96.2 Ω and 77.8 Ω at $T = 280$ K for Sub. = STO and $SiO_2$/Si, respectively, which is nearly 8-fold larger than that in sample with Sub. = SR-STO ($R_s \approx 12.2$ Ω). In particular, $R_s$ drops rapidly with decreasing temperature for Sub. = SR-STO, giving a $R_s$ of about 12 mΩ at $T = 10$ K, which is more than three orders of magnitude lower than that in Sub. = STO and $SiO_2$/Si at similar temperature. Such a low $R_s$ at lower temperatures in Sub. = SR-STO indicates a highly conducting nature in the SR-STO, and the electron–phonon scattering plays a crucial role, giving rise to a rapid drop of more than three orders of magnitude in $R_s$ as temperature goes from 300 K to 10 K. Therefore, Al(1 nm)/Nb (10 nm)/SR-STO shall be considered as an interesting system of superconducting layer proximity coupled to a highly-conducting SR-STO substrate with a strong electron–phonon coupling. Figure 2b plots the normalized sheet resistance $R_s/R_n$ versus $T$ near the superconducting transition for samples with $d = 10$ nm. We adopted the convention by taking the superconducting transition temperature $T_c$ as the temperature with $R_s/R_n = 1/2$. The $T_c$ equals 4.6 K and 4.9 K for Sub. = STO (blue line in Fig. 2b) and Sub. = $SiO_2$/Si (red line), while $T_c$ for Sub. = SR-STO (black line) is apparently higher with a value of 6.2 K. The detailed thickness dependence on the $T_c$ is shown in Fig. 2c, where the Nb thickness was *in-situ* monitored by a quartz crystal microbalance. The control samples of Sub. = $SiO_2$/Si with different thicknesses follow a simple relation of $\log(T_c) \propto 1/d$, which is consistent with some earlier works[19]. We remark that samples of Sub. = SR-STO (star symbols and open triangles in Fig. 2c) turn out to show higher $T_c$ compared to control samples (circles and diamonds) with the same Nb thickness, where the difference in $T_c$ appears to be larger for thinner Nb layer (smaller $d$).

The upper critical field $H_{c2}$ can be readily obtained from the field dependence of sheet resistance $R_s(H)$ and Hall resistance $R_{xy}(H)$ at temperatures ranging from 2 K to 7 K as shown in Fig. 3a for Al(1 nm)/Nb(10 nm)/SR-STO sample with a field perpendicular to the film surface. The extracted $H_{c2}$ as a function of the reduced temperature ($T/T_c$) is shown as black squares in Fig. 3b, where the results for control samples of Sub. = STO (blue circles) and $SiO_2$/Si (red diamonds) were also included for comparison. For Sub. = SR-STO at $T/T_c \approx 0.4$, $\mu_0 H_{c2,\perp}$ ($H \perp$ ab) and $\mu_0 H_{c2,\parallel}$ ($H \parallel$ ab) equal 2.24 T and 10.88 T, respectively. The effective superconducting layer thickness $d_{GL}$ and also zero temperature Ginzburg-Landau (GL) superconducting coherence length $\xi_{GL}(0)$ can be estimated from the $H_{c2}$ anisotropy based on the GL theory of $\mu_0 H_{c2,\parallel} = \frac{\sqrt{3}\Phi_0}{d_{GL}\pi\xi_{GL}(0)}\sqrt{1-\frac{T}{T_c}}$ and $\mu_0 H_{c2,\perp} = \frac{\Phi_0}{2\pi\xi^2_{GL}(0)}(1-\frac{T}{T_c})$[20], where $\Phi_0$ is the flux quantum. The extracted $d_{GL}$ and $\xi_{GL}(0)$ values are summarized in Table 1. For Sub. = SR-STO and $d = 10$ nm, effective thickness $d$ is about 8.5 nm that is about 10% lower than that for control samples. On the other hand, $\xi(0)$ equals 9.3 nm, which is about 10% higher than that for control samples. Similar behavior is

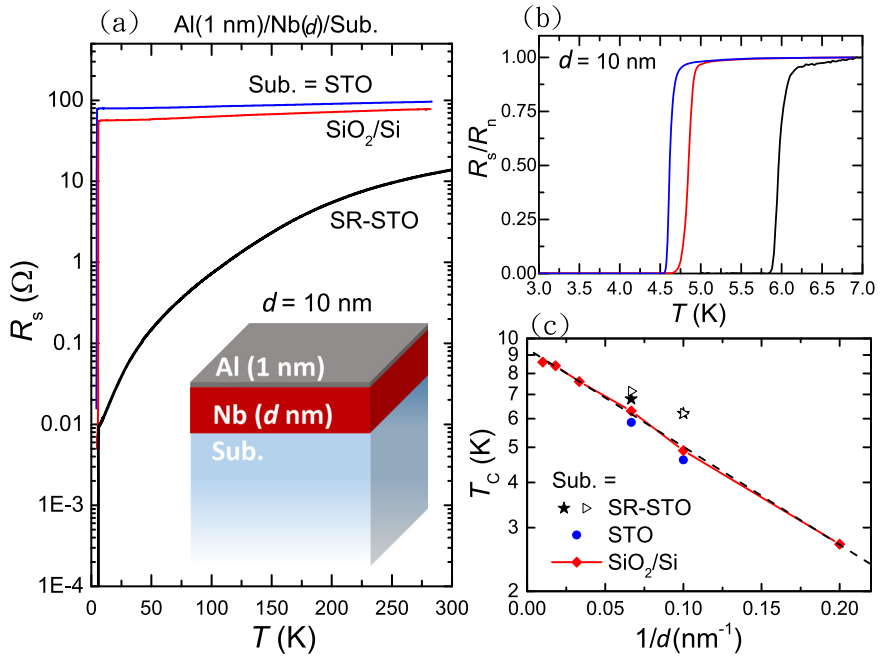


**Fig. 2 The sheet resistance data. a** The temperature dependence of the sheet resistance $R_s$ in a logarithmic scale for Al(1 nm)/Nb(10 nm)/Sub. with three different substrates of STO, $SiO_2$/Si, and SR-STO. For Sub. = SR-STO, $R_s$ is nearly an order of magnitude smaller at room temperature, and it rapidly decreases with decreasing temperature, giving a mere $R_s \approx 10\,m\Omega$ at around 10 K. The inset cartoon of **a** illustrates the device composition. **b** The normalized sheet resistance $R_s/R_n$ as a function of temperature below 7 K. The blue and red lines are the curves for Al (1 nm)/Nb(10 nm)/STO and Al(1 nm)/Nb(10 nm)/$SiO_2$/Si samples, respectively, showing lower superconducting transition temperatures as compared to that in Al(1 nm)/Nb(10 nm)/SR-STO. **c** The superconducting transition temperature $T_c$ in log scale versus $1/d$, where $d$ is the thickness of the Nb layer. The phenomenological dependence of log ($T_c$) $\propto 1/d$ is well observed in samples with Sub. = $SiO_2$/Si. $T_c$ appears to be higher in samples with Sub. = SR-STO (star symbols and open triangles).

found in $d = 15$ nm samples. We do note that $d_{GL}$ values are close to but somewhat smaller than the nominal thickness $d$ determined from the quartz crystal microbalance. The magnetoresistance (MR) data of Al(1 nm)/Nb(10 nm)/Sub. are shown in Fig. 3c with green and black lines for transverse MR ($H \perp$ ab) and longitudinal MR ($H \parallel I$), respectively. A large positive transverse and longitudinal MR with a magnitude of 251% and 86%, respectively, at $\mu_0 H = 10$ T are observed in the sample with Sub. = SR-STO (left panel of Fig. 3c), which is more than two orders of magnitude larger than that in samples with Sub. = $SiO_2$/Si (middle panel) and Sub. = STO (right panel). We also remark that the negative Hall slope in sample with Sub. = SR-STO (Fig. 3a lower panel at 7 K) indicates dominant electron-like carriers, which is opposite to the hole-like carriers found in control samples with Sub. = STO and $SiO_2$/Si (see Supplementary Fig. 2).

As shown in Fig. 3b, the upper critical field $H_{c2}$ for $H \parallel I$ can be more than 10 Tesla at lower temperatures. An unusual field-induced resistance peak was uncovered near the superconducting transition, which is absent in zero field and tends to grow larger in magnitude with field strength. Fig. 4a shows the $R_s - H$ curves at temperature varying from 2 K to 7 K, where the inset cartoon illustrates the field orientation of $H \parallel I$. For $T \le 5$ K, a pronounced resistance peak was observed when the system passes from a superconducting state to a normal state via field sweeping, and the magnitude of resistance peak grows with increasing field strength. On the other hand, such a resistance peak can also be observed by temperature sweeping across the superconducting transition as shown in Fig. 4b with field ranging from 0 T to 12 T. For $\mu_0 H \ge 2.5$ T, $R_s$ starts to rise up as the temperature drops below an onset temperature ($T_{on}$), and it then reaches a local maximum at $T_p$ before quickly entering the superconducting state with vanishing $R_s$. The relative magnitude of the resistance peak ($\Delta r$) for Al(1 nm)/Nb($d$)/SR-STO with $d = 10$ nm (open symbols) and 15 nm (closed symbols) with two different field geometries of $H \parallel I$ (circles) and $H \parallel$ ab $\perp I$ (squares) are summarized in Fig. 4c, where the inset figure of Fig. 4c illustrates the definitions of the $T_{on}$, $T_p$, and $\Delta r$ we used in the discussions. In general, $\Delta r$ is zero at low fields, and it starts to appear above a certain field, where $\Delta r$ grows practically linear with field strength up to more than 10 T. $\Delta r$ can be as large as 0.56 at $\mu_0 H = 8.5$ Tesla for $d = 15$ nm with $H \parallel$ ab $\perp I$. In the sample of $d = 15$ nm with $H \parallel I$, we note that $\Delta r$ decreases with increasing field for $5 \le \mu_0 H \le 7.5$ T, where the corresponding $T_p$ turns out to shift to a lower temperature (see Supplementary Fig. 1), and thus the peak resistance effect was largely reduced by the rapid drop in $R_s$ at $T_c$. From those observations, we constructed a unique $H$–$T$ phase diagram for the proximity coupled superconducting system of Al(1 nm)/Nb($d$)/SR-STO, which is shown in Fig. 4d for $d = 10$ nm with $H \parallel I$. The color code in Fig. 4d corresponds to the value of normalized sheet resistance of $R_s/R_n$. Other than the regular phase boundary of $T_c$ (yellow line) between the normal state (light gray color) and superconducting state (black color), there is a white region between the $T_{on}$ (blue-dashed line) and $T_c$ lines, representing the appearance of unique peak resistance effect. The $T_p$ line is found to be close to $T_c$ line at higher fields. It gradually moves toward the $T_{on}$ line as $H$ reduces and meets with $T_{on}$ line at about $\mu_0 H = 2.5$ T, below which the peak resistance effect completely disappears.

## DISCUSSION

Similar resistance peak phenomena have been reported before in several systems, such as mesoscopic superconducting nanowires, disordered superconductors, and anisotropic superconducting systems. A large resistance peak was observed at zero field in several cuprates, including $La_{2-x}Sr_xCuO_4$, $Bi_2Sr_2CaCu_2O_8$, and $YBa_2Cu_3O_7$[21–23], which has been attributed to either the interplane vortex effect or the resistivity and thus $T_c$ anisotropy in those layered superconductors. Simulations, based on the measured

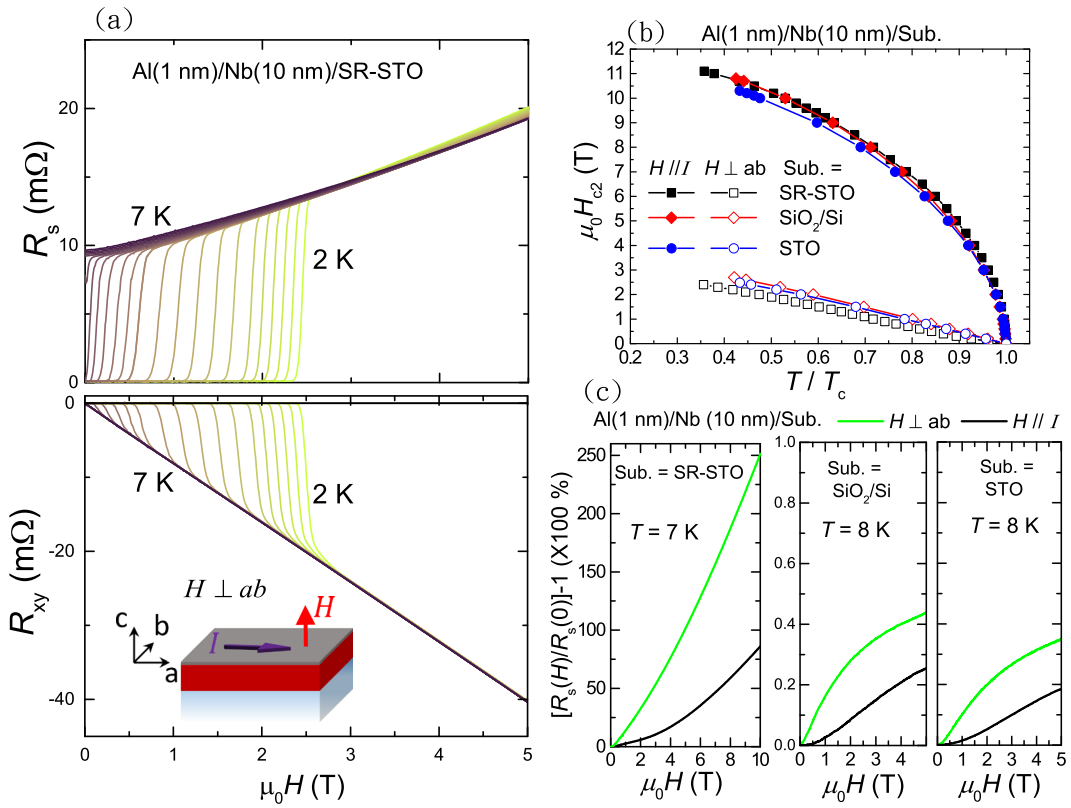


**Fig. 3 The magneto-transport data.** The upper and lower panels of **a** show the field dependence of the sheet resistance $R_s$ and Hall resistance $R_{xy}$, respectively, in Al(1 nm)/Nb(10 nm)/SR-STO sample at temperature varying from 2 K to 7 K. The field is applied perpendicular to the film surface as illustrated in the inset figure of the lower panel. **b** The field anisotropy of upper critical field $H_{c2}$ as a function of reduced temperature $T/T_c$ for samples using different substrates of SR-STO, $SiO_2$/Si, and STO. **c** A comparison of the magnetoresistance (MR) in the normal state. The green and black lines are the MR curves with field perpendicular to the film surface and field parallel to the in-plane current direction, respectively. A large positive MR was observed in the sample with Sub. = SR-STO (left panel), which is more than two orders of magnitude larger than that with Sub. = $SiO_2$/Si (middle panel) and Sub. = STO (right panel).

**Table 1.** The GL parameters for Al(1 nm)/Nb(*d*)/Sub. samples.

| | $d = 10$ nm | | $d = 15$ nm | |
|---|---|---|---|---|
| Sub. | $d_{GL}$(nm) | $\xi_{GL}(0)$(nm) | $d_{GL}$(nm) | $\xi_{GL}(0)$(nm) |
| SR-STO | 8.5 | 9.3 | 10.1 | 9.2 |
| STO | 9.5 | 8.6 | 11.0 | 8.1 |
| $SiO_2$ | 9.3 | 8.4 | 10.5 | 8.0 |

difference in resistivity and $T_c$ with a current either along or perpendicular to the layer, do reproduce such a resistance peak feature in the *R*–*T* curve[24]. We thus performed a control experiment by measuring the *R*–*T* behavior in Nb/SR-STO samples with currents applied along two different substrate crystalline axes. The difference in $T_c$ and transition width is negligible, and we thus exclude the possibility of field-induced in-plane anisotropy for the occurrence of resistance peak. We also note that the resistance peak we observed in Nb/SR-STO is not likely due to an inhomogeneous current distribution, since the *R*–*T* profiles can be well reproduced regardless of the voltage leads geometry and location (see Supplementary Fig. 3 and Fig. 4). On the other hand, resistance peak in a mesoscopic superconducting wire is typically associated with the formation of superconductor-normal metal-superconductor (SNS) junction and possible enhanced phase-slips[25,26]. In this case, the resistance peak appears to be the largest in zero field, and its magnitude got suppressed rapidly by a small external fields. This is the opposite of what we observed in our Nb/SR-STO samples, in which the resistance peak is absent in zero field and grows larger with field intensity as shown in Fig. 4c. The fact that the resistance peak is much more pronounced with in-plane fields also precludes the role of vortex effect. A number of reports also showed pronounced resistance peaks at zero field in disordered or granular superconductors[27,28], where a possible localized Cooper pair state due to disorder is proposed. This is incompatible to the absence of the resistance peak in zero field found in our Nb/SR-STO samples. In addition, the atomic force microscope and low angle reflectivity measurements reveal a relatively smooth surface and a macroscopic uniformity of our Nb film thickness, respectively (see supplementary Fig. 5). Therefore, disordered effect is less likely to be important in our Nb/SR-STO samples, and other new mechanism is needed to explain the resistance peak phenomenon found in our Nb/SR-STO system.

## DFT calculations of electronic structure of SR-STO

A similar behavior was reported in mesoscopic devices, comprising superconducting electrodes proximity coupled by a ferromagnetic nanowire[29]. The resistance peak was found to survive under intense magnetic field, and the magnetism in the ferromagnetic wire was inferred to play a crucial role. In systems with a single oxygen vacancy, previous DFT results have shown that the interplay between the local $C_4$ symmetry breaking on Ti atom near the oxygen vacancy and the Hubbard *U* interaction leads to in-gap states with local moments and a Rashba-like spin texture[6–8]. Furthermore, it has been reported that DFT with dynamical mean-field theory (DMFT) predicts strong tendency toward ferromagnetic ordering in the presence of two oxygen vacancies. In light of this result, we performed DFT calculations using the Perdew-

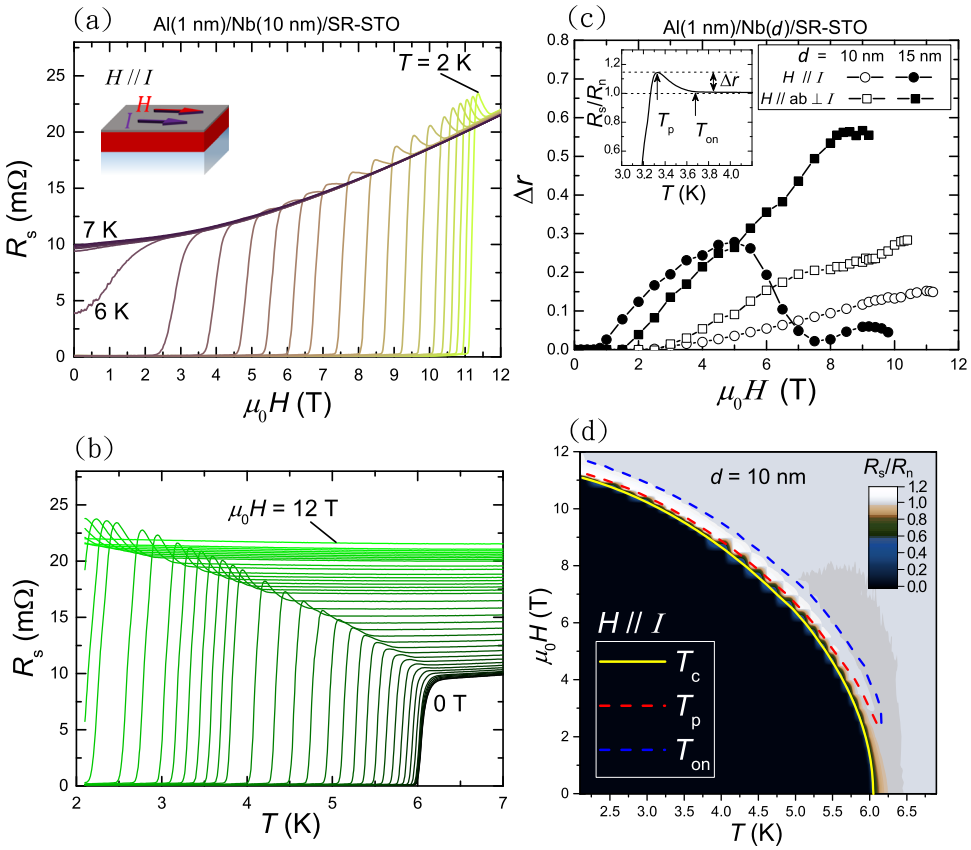


**Fig. 4 The peak resistance effect. a** The field dependence of $R_s$ at temperatures ranging from 2 K to 7 K in Al(1 nm)/Nb(10 nm)/SR-STO sample. **b** The temperature dependence of $R_s$ at fields ranging from 0 to 12 T. Pronounced field-induced resistance peaks are shown in **a**, **b**. The relative magnitude of the resistance peak $\Delta r$ as a function of the field strength is shown in (**c**). Solid and open symbols are results for $d =$ 15 nm and 10 nm, respectively. The upper left inset figure illustrates the definitions for the peak temperature $T_P$, onset temperature $T_{on}$, and $\Delta r$. $\Delta r$ practically increases with increasing field without saturation, except for $d = 15$ nm sample with $H \| I$. See main text for more descriptions. **d** The $H$–$T$ phase diagram of the Al(1 nm)/Nb(10 nm)/SR-STO system. The blue-dashed and red-dashed lines are the extracted $T_{on}$ and $T_P$ values, respectively. The color code represents the normalized sheet resistance ($R_s/R_n$) of the sample with light-gray and black regions for normal state and superconducting state, respectively. The white region between the blue-dashed line and yellow-solid line ($T_c$) is an unusual state with resistance peaks uncovered in the Al(1 nm)/Nb($d$)/SR-STO system.

Burke-Ernzerhof (PBE) generalize gradient approximation (GGA) functional[30] with the Hubbard $U$ correction in the WIEN2k software package[31] to explore the possible magnetism arising from the SR-STO. Using the $TiO_2$-terminated STO, we created the surface unit cells shown in Fig. 5a, d with a depth of 5 $TiO_2$ slabs in the low-temperature tetragonal structure, we simulated the patterned oxygen vacancies in order to study the vacancy effects on the surface of STO. In our results presented, we considered a $5 \times 5 \times 1$ $k$-mesh and included spin-orbit coupling along the [001]-direction with $U = 2$ eV. We performed the calculations for both paramagnetic and ferromagnetic states and found the ferromagnetic state to always be the ground state. We also tested different magnetization axes for the spin-orbit coupling ([100] and [010]) and found no discernible difference in the total energies. Additionally, we tested $U = 1$, 2, 3, and 4 eV and found our results were consistent for the entire range of $U$ used. From our calculations, we found a strong non-zero net magnetic moment ($\frac{1}{2}(n_\uparrow - n_\downarrow)$) on the surface of our SR-STO unit cell. To identify the root of this net moment, we first calculated the projected density of states (PDOS) for the Ti atoms at the surface of our SR-STO unit cell with this initial spin arrangement and compared it with the total density of states of our unit cell (Fig. 5b and e). From this, we see the onset of an in-gap peak, as was reported previously[6,7], which can be mostly attributed to the Ti atoms on the surface as well as a larger population of the spin-up electronic states, similar to the two oxygen vacancy case[32]. Our GGA+U simulations reveal that the highest spin densities are found at Ti atoms near the vacancy sites and decreasing for atoms further from the vacancies. Those results are consistent with the picture proposed by Lin and Demkov that the magnetism is induced by the local orbital mixing due to the oxygen vacancy[7]. Since our system forms a global vacancy pattern, this spin density distribution forms spin density wave states, which can be seen in Fig. 5c, f. The formation of spin density wave (SDW) states leads us to conclude that the system may be close to the ferromagnetic long-range order, which tends to compete with the superconducting order of the proximity-coupled Nb.

## Magnetic property of SR-STO and interface resistance between superconductor and ferromagnet

We carried out comprehensive magnetization measurements on Al(1 nm)/Nb($d$)/SR-STO samples and also a control sample of STO without surface reconstruction for comparison. The upper panel of Fig. 6a shows the magnetization ($M$), normalized to the surface area of the substrate, as a function of in-plane magnetic field ($H$ // ab) for Al(1 nm)/Nb(10 nm)/SR-STO sample at $T = 10$ K and 300 K, and the $M$–$H$ curve for the control sample of STO at 10 K is shown as blue lines. For $|\mu_0 H| \geq 0.1$ T, the magnetic signal is dominated by the diamagnetic moment from the bulk STO, making it difficult to extract the surface magnetic moment contribution in the high

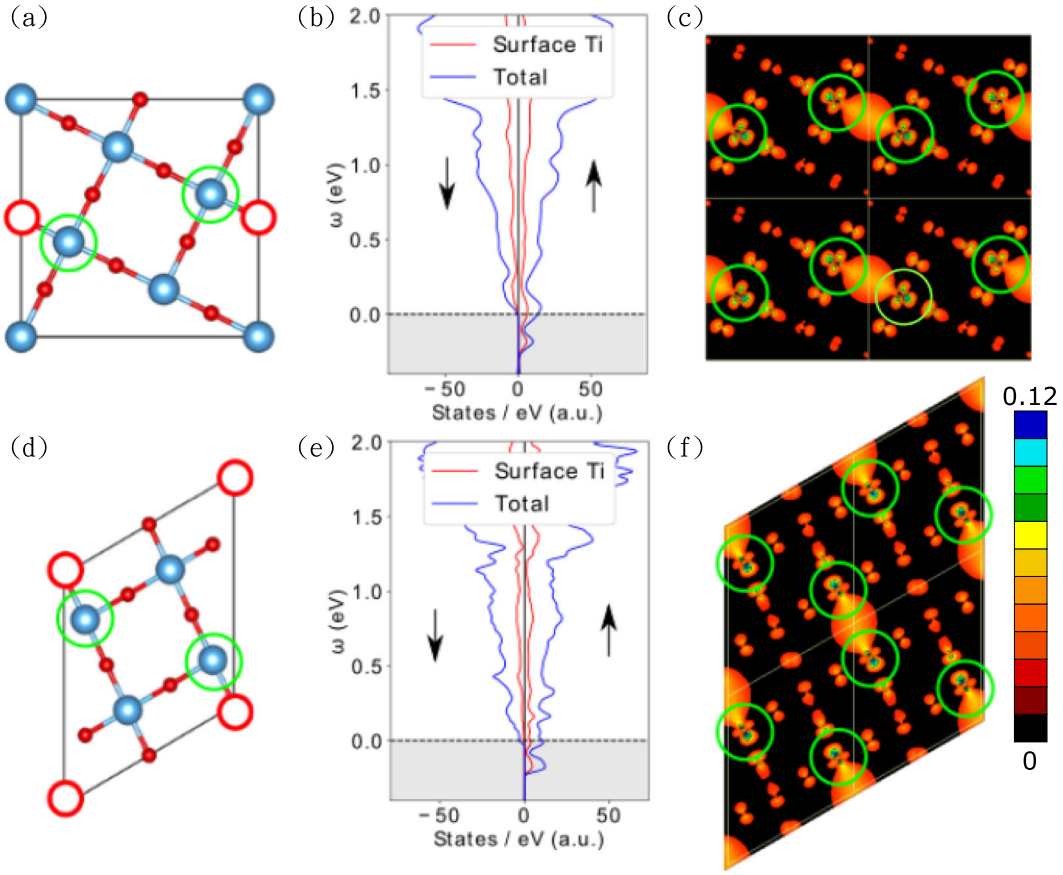


**Fig. 5 The DFT calculations. a–c** Refer to the $\sqrt{5}\times\sqrt{5}$ R26.6° structure and **d**-**f** refer to the c(4 x 2) structure. **a**, **d** show the surface unit cells, where the open red circles indicate the locations of the oxygen vacancies in the unit cell. All calculations were done with a structure having 5 $TiO_2$ planes thick. **b**, **e** show the DOS for the SR-STO structure with U = 2 eV in comparison with the total DOS to show the onset of the spin-polarized in-gap peaks for the surface Ti atoms. The shaded region in each plot shows the energy range used in calculating the spin densities. Finally, **c**, **f** show the net spin densities for the surface of our SR-STO unit cells, directly correlating with the net magnetic moment due to states in the energy range shaded in **b**, **e**. The color bar represents the values of local magnetic moment calculated from DFT. The regions indicated by the green circles are referencing the Ti sites neighboring the vacancies, as in the surface unit cells in **a**, **d**. By expanding the visible area to $2\times2$ unit cells in the *x* and *y* directions, we can see that the presence of periodic, patterned oxygen vacancies leads to the appearance of a spin density wave.

field regime. We thus focus on the weak field regime, where the diamagnetic background is vanishing small. The apparent hysteresis loop indicates the presence of a ferromagnetic-like magnetic signal that persists up to 400 K (see Supplementary Fig. 6). The corresponding differential susceptibility $\chi = dM/dH$ is plotted in the lower panel of Fig. 6b, where the data for Al(1 nm)/Nb(10 nm)/SR-STO at $T = 300$ K and STO control sample at 10 K were shifted upward and downward by a magnitude of 0.2 $\mu$ emu $cm^{-2}$ $G^{-1}$, respectively, for clarity. The red open circles and blue open squares represent the data points with opposite *H* sweeping directions, indicating by the arrows in the figure. The coercive field $H_c$ for Al(1 nm)/Nb(10 nm)/SR-STO, extracted from the local maximum in *dM*/*dH*–*H* curve, equals ≈ 35 mT at $T = 10$ K, and it reduces to about 7 mT at $T = 300$ K. By integrating the *dM*/*dH*–*H* curve, the shaded area shown in the lower panel can be obtained, giving the weak-field magnetization ($M_{LH}$) for the ferromagnetic-like contribution. The extracted $M_{LH}$ in four different samples were summarized in Fig. 6b with two different field orientations of *H*// ab (left panel) and $H \perp$ ab (right panel). The control sample of STO without surface reconstruction was found to give the lowest $M_{LH}$ of ≤50 $\mu$ emu $cm^{-2}$ (shaded area in Fig. 6b). It can be attributed to minute magnetic impurities of a level ≤1 ppm in STO (e.g., 1 ppm $Fe^{3+}$ ions give about 200 emu $cm^{-2}$ with a substrate thickness of 0.05 cm). For other samples using SR-STO as substrate, the weak field $M_{LH}$ is at least two-fold larger than that in the control sample of STO without surface reconstruction. For Al(1 nm)/Nb(10 nm)/SR-STO at $T = 10$ K, $M_{LH}$ is about 245 and 144 emu $cm^{-2}$ for $H$ // ab and $H \perp$ ab, respectively, and $M_{LH}$ values do not vary significantly up to 300 K. We also note that similar magnetic behavior was observed for Al(3 nm)/SR-STO sample without Nb layer, suggesting the weak field $M_{LH}$ is intrinsic and deriving from the SR-STO. In Fig. 6c, the corresponding $H_c$ values are shown with magnitude less than 50 mT. Those results agree with the possible SDW phase from our DFT calculation and also several earlier reports on the surface magnetism in oxygen-deficient STO (for a review, please refer to ref. [33]). The origin of such an intrinsic weak field $M_{LH}$ remains a debatable issue, where complex spin coupling between the in-gap spin-polarized states and the itinerant *d* electrons may play an important role. We also notice that, for Al(1 nm)/Nb (15 nm)/SR-STO, the $M_{LH}$ is much reduced at a lower temperature for $H \perp$ ab, which is most likely associated with the presence of magnetic anisotropy at lower temperatures.

Based on the existence of such an intrinsic ferromagnetic-like magnetism in SR-STO, the physical phases in Al(1 nm)/Nb(*d*)/SR-STO system can be illustrated by a cartoon shown in Fig. 7a, where the horizontal (blue) arrows represent the magnetization with a declining magnitude as moving away from the Nb/SR-STO interface. Within a thickness of about $\xi_h = \sqrt{D/h}$ (*D* and *h* are

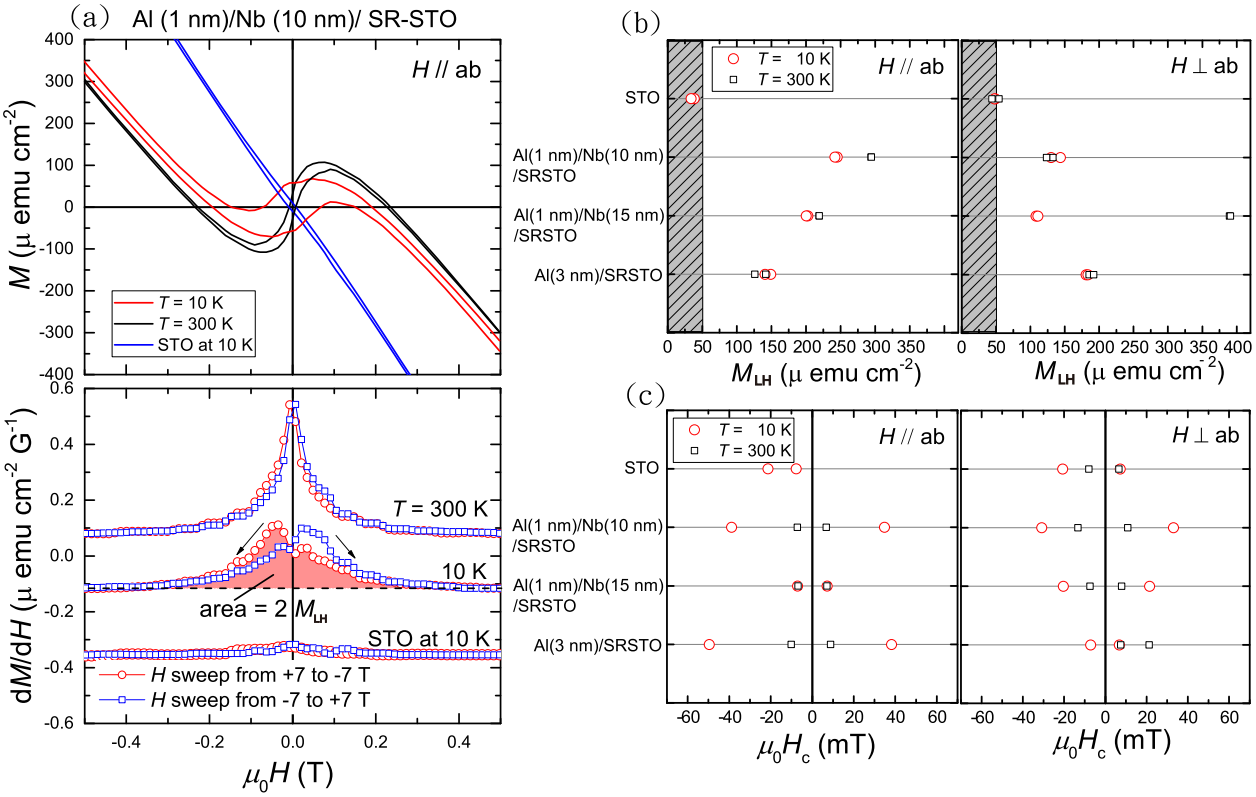


**Fig. 6 The magnetization data.** The upper panel and lower panel of **a** show the magnetization and differential susceptibility $\chi = dM/dH$, respectively, as a function of in-plane magnetic field ($H$ // ab) for Al(1 nm)/Nb(10 nm)/SR-STO sample. A Large weak field hysteresis loop was observed, which persists up to 300 K, which is in big contrast to the much smaller loop for the control sample of STO without surface reconstruction (blue lines). The shaded area in the lower panel can be obtained by integrating the $dM/dH$–H curve, giving the weak field magnetization ($M_{LH}$). The $dM/dH$–H curves for $T = 300$ K and STO without surface reconstruction at 10K were shifted for clarity. **b**, **c** Show the summaries of the extracted $M_{LH}$ and the corresponding coercive field $H_c$, respectively, for four different samples at $T = 10$ K and 300 K with different field orientations of $H$ // ab (left panel) and $H \perp$ ab (right panel). See the main text for more details.

the diffusion coefficient and exchange field, respectively, of the ferromagnet[34]), there is a proximity-induced superconducting regime on the SR-STO side, which forms a superconductor/ferromagnet (SC/FM) interface shown as green dashed line in the cartoon. Considering a one dimensional spin diffusion model across a SC/FM interface, the boundary conditions at the interface require both $\mu_\uparrow(x = 0) = -\mu_\downarrow(x = 0)$ and $j_\uparrow(x = 0) = j_\downarrow(x = 0)$ due to constraints from Andreev reflection effect and zero net spin current on SC side[35] (Fig. 7b), where $\mu_{\uparrow(\downarrow)}$ is the chemical potential for spin up (down) electrons, and spin current density $j_{\uparrow(\downarrow)} = -(\sigma_{\uparrow(\downarrow)}/e)\partial\mu_{\uparrow(\downarrow)}/\partial x$. The SC/FM interface resistance can be expressed as $R_i = \Delta\mu/ej = [p^2/(1-p^2)](\rho_F\lambda^F_{SF})$[29,35], where $p = (\sigma_\uparrow - \sigma_\downarrow)/(\sigma_\uparrow + \sigma_\downarrow)$ and $\rho_F$ ($\lambda^F_{SF}$) are the spin-polarization and resistivity (spin-diffusion length), respectively, of the FM. For $T < T_c$, the SC/FM interface is located within the SR-STO, and it disappears as the temperature goes above $T_c$. A simplified resistor network model for the Al(1 nm)/Nb($d$)/SR-STO system can then be constructed and shown in the inset cartoon of Fig. 7c. As $T$ increases across the superconducting transition, $R_i$ transforms from the resistance of a SC/FM interface to that of a metal/FM interface, and the interface resistance changes across $T_c$ can be expressed as

$$\Delta R_i = R_i(T < T_c) - R_i(T > T_c) = \frac{fp^2}{(1-p^2)(1-p^2+f)}\rho_F\lambda^F_{SF}, \qquad (1)$$

where $f = \rho_F\lambda^F_{SF}/\rho_N\lambda^N_{SF}$ and $\rho_N$ ($\lambda^N_{SF}$) is the resistivity (spin diffusion length) of the Nb in normal state. We remark that $\Delta R_i$ is always positive and diverges as $p$ approaches one that corresponds to a fully spin-polarized state in the FM. We then model a step-like function for the temperature dependent interface resistance of $R_i(T) = A/(e^{-w/R_{Nb}} + 1) - C$, where $A$, $w$ and $C$ are some constants, and $R_{Nb}$ is the sheet resistance of the Nb thin film from the control sample using $SiO_2$/Si as a substrate. As an example in Fig. 7c, the simulated effective sheet resistance ($R_{eff}$) of the resistor network (blue line), using $R_i(T)$ and the the corresponding $R_{Nb}$ and $R_{SR-STO}$ from control samples, can reasonably reproduce the resistance peak feature found in the experimental $R_s$ data (open circles) of Al (1 nm)/Nb(10 nm)/SR-STO sample. Nevertheless, considering the macroscopic junction area (~1 mm$^2$) in our samples, the simulated SC/FM interface resistance $R_i$ of about 2.2 mΩ turns out to be only possible with a fully spin-polarized state in the FM ($1 - p \le 10^{-6}$) if we take $\rho_F = 0.01\ \Omega \times 10^{-5}$ cm and $\lambda^F_{SF} = 10^{-5}$ cm. It is not clear whether a field-enhanced exchange coupling for the in-gap states can lead to such a fully spin-polarized state. While more complex model than resistor network may be required, further investigations are also needed to reveal the spin-polarization and other spin-related parameters near the surface of a SR-STO under magnetic field.

To justify the resistor network model, we construct a SC/FM/SC layered tight-binding model shown in the upper panel in Fig. 7d to investigate the conductance across the SC/FM interface. To minimize the finite size effect, a periodic boundary condition between SC layers on both sides is introduced. The ferromagnetism is introduced by the spin-dependent chemical potential $\mu_\sigma = E_F - \sigma M$, where $M$ is the ferromagnetic order parameter. In SC layers, the superconducting gap $\Delta$ is introduced via the standard BCS mean-field pairing Hamiltonian. The interface is modeled by the barrier potential $V_b$ which is similar to the $Z$ parameter used in the Blonder-Tinkham-Klapwijk (BTK) formalism[36]. The

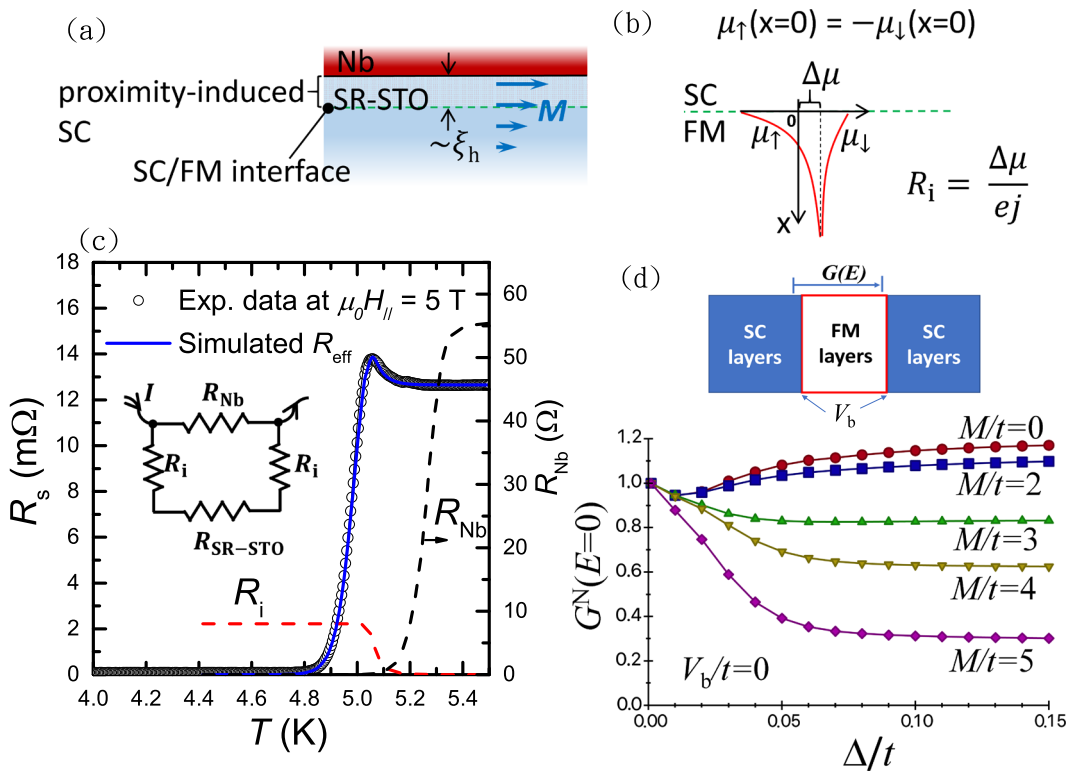


**Fig. 7 The resistor network model with SC/FM interface resistance. a** An illustration of the proximity coupled Al(1 nm)/Nb(*d*)/SR-STO system. The blue horizontal arrows represent the magnetization in SR-STO, and the green dashed line is an SC/FM interface between the proximity-induced SC region and the rest of SR-STO. **b** The spin-up (spin-down) chemical potential $\mu_{\uparrow(\downarrow)}$ across a SC/FM interface, and x is the distance to the interface. A boundary condition of $\mu_\uparrow(x=0) = -\mu_\downarrow(x=0)$ was introduced to respect the constraint due to the Andreev reflection effect. The interface resistance $R_i = \Delta\mu/ej$ can then be determined using a one dimensional spin diffusion model. A simplified resistor network model is shown in the inset cartoon of (**c**). The resistance peak feature for the Al(1 nm)/Nb(10 nm)/SR-STO with an in-plane field of $\mu_0 H = 5$ T is well reproduced by the simulated effective resistance $R_{eff}$ of the proposed resistor network (blue line). The dashed black and red lines are the corresponding $R_{Nb}$ and $R_i$ for the simulated $R_{eff}$. The geometry of the SC/FM/SC layered model is shown in the upper panel of (**d**). There are $N_1$ layers for SC on both sides and $N_2$ layers for FM. The lower panel of **d** shows the normalized zero-energy conductance $G^N(\Delta, E=0)$ in the transparent limit.

tight-binding Hamiltonian can be written as

$$\begin{aligned}
\hat{H} &= \hat{H}^{FM} + \hat{H}^{L}_{SC} + \hat{H}^{R}_{SC},\\
\hat{H}^{FM} &= \sum_{k\sigma}\sum_{z=z'}^{z''}\left[\epsilon^{FM}(k) - \mu_\sigma + (\delta_{z,z'} + \delta_{z,z''})V_b\right]c^\dagger_{k,z,\sigma}c_{k,z,\sigma}\\
&\quad + (-tc^\dagger_{k,z,\sigma}c_{k,z+1,\sigma} + h.c.),\\
\hat{H}^{L}_{SC} &= \sum_k\sum_{z=1}^{N_1}\sum_\sigma(\epsilon^{SC}(k) - E_F)c^\dagger_{k,z,\sigma}c_{k,z,\sigma}\\
&\quad + (-t_{SC}c^\dagger_{k,z,\sigma}c_{k,z+1,\sigma} + h.c.) + (-\Delta c^\dagger_{k,z,\uparrow}c^\dagger_{-k,z,\downarrow} + h.c.),\\
\hat{H}^{R}_{SC} &= \sum_k\sum_{z=z''+1}^{2N_1+N_2}\sum_\sigma(\epsilon^{SC}(k) - E_F)c^\dagger_{k,z,\sigma}c_{k,z,\sigma} + (-t_{SC}c^\dagger_{k,z,\sigma}c_{k,z+1,\sigma} + h.c.)\\
&\quad + (-\Delta c^\dagger_{k,z,\uparrow}c^\dagger_{-k,z,\downarrow} + h.c.),
\end{aligned} \tag{2}$$

where there are $N_1$ layers for SC at both sides and $N_2$ layers for FM, $z' = N_1 + 1$ and $z'' = N_1 + N_2$ are the layer indices for the interfacial layers, $k$ is the in-plane momentum, $\epsilon^{FM} = -2t(\cos k_x + \cos k_y)$, and $\epsilon^{SC} = -2t_{SC}(\cos k_x + \cos k_y)$. With this Hamiltonian, we can use the Landauer formula to compute the conductance between layers $i$ and $j$:

$$\begin{aligned}
G_{ij}(E) &= \tfrac{2e^2}{h}\textstyle\sum_k T^k_{ij}(E)\,,\ T^k_{ij}(E) = |\mathcal{G}^R_{ij}(E,k)|^2,\\
\mathcal{G}^R_{ij}(E,k) &= \left[(E+i\eta)\hat{I} - \hat{H}_k\right]^{-1}_{ij},
\end{aligned} \tag{3}$$

where $T^k_{ij}(E)$ is the transmission probability from layer $i$ to $j$ with in-plane momentum $k$, and $\mathcal{G}^R_{ij}(E,k)$ is the corresponding retarded Green's function. We compute the conductance from $i = z' - 1$ (the last layer of SC on the left) to $j = z''$ (the last layer of FM), as shown in the upper panel of Fig. 7d to capture the Andreev reflection near the SC/FM interface. In all the calculations presented here, we put $N_1 = N_2 = 200$ and $t_{SC}/t = 4$.

We focus on the conductance at zero energy, which corresponds to the resistance used in the resistor network model ($R_i \sim 1/G(0)$). In the lower panel of Fig. 7d, we plot the zero-energy conductance normalized to the normal state one, defined as $G^N(\Delta, E=0) \equiv G_{ij}(\Delta, E=0)/G_{ij}(\Delta=0, E=0)$, as a function of Δ with ($V_b$, $M$) fixed. Since our sample is likely to be in the transparent limit, we set $V_b = 0$ in the calculation. It is confirmed that the normalized zero-energy conductance across the SC/FM interface for the FM layers with large $M$ always decreases with Δ and saturates to a certain value for large Δ, due to the suppression of the Andreev reflection by the spin polarization. On the contrary, for small $M$ the normalized zero-energy conductance increases with Δ, because the Andreev reflection remains robust for small spin polarization. Since from the BCS theory $\Delta(T) \propto \Delta(T=0)\sqrt{1 - T/T_c}$, our calculation suggests that the zero-energy interfacial conductance for the FM layers with large spin polarization will monotonically decrease with the temperature below $T_c$, which justifies the step-like temperature profile of the interfacial resistance $R_i$ proposed in the resistor network model.

We further fabricated superconductor/SR-STO heterostructure using different superconducting layers of lanthanum (La) and aluminum (see Supplementary Fig. 7). Similar resistance peak phenomenon was observed in La(20 nm)/SR-STO sample, and the magnitude of resistance peak (Δ*r*) increases with increasing

in-plane field strength, which is in accord with the field-induced resistance peak in Al(1 nm)/Nb(*d*)/SR-STO samples. However, we do notice that Δ*r* is nearly 5-fold smaller as compared to Nb (10 nm)/SR-STO sample at similar field strength. Such a notable variation in Δ*r* at similar field strength may be attributed to the difficulty in the experimental control over the interface quality and thus the barrier potential ($V_b$) that can affect the interface resistance, according to the DFT calculations (Fig. 7d).

We studied the superconducting property in proximity coupled Al(1 nm)/Nb(*d*)/SR-STO system. With proper preparations, SR-STO substrates with surface structures of $\sqrt{5}\times\sqrt{5}$ *R*26.6° and c(4 × 2) can be well reproduced, and the corresponding electronic property not only exhibits strong electron–phonon coupling effect but also shows intriguing spin-polarized in-gap states based on the DFT calculations. While those spin-polarized states do not give a long-range magnetic order in weak fields, a larger field can, in principle, promote the long-range magnetic order in SR-STO, making it an intriguing example of proximity coupled superconductor/ferromagnet bilayer. We uncovered a notable region in the *H*–*T* phase diagram, showing unusual resistance peak phenomenon. Such a field-induced resistance peak can be attributed to the proximity coupling of the superconducting Nb to the spin-polarized in-gap states with possible field-assisted long-range magnetic order. By using a simplified resistor network model with a step-like interface resistance ($R_i(T)$), the resistance peak behavior can be explained, and the extracted $R_i$ value for SC/FM interface is on the order of a few mΩ that may infer a fully spin-polarized FM state in the SR-STO under magnetic field. Similar resistance peak phenomenon was also observed using La as the superconducting layer, justifying the generic feature of the peak resistance effect in a superconductor/SR-STO heterostructure. Our work provides an intriguing way of revealing the unusual electronic states in the SR-STO due to oxygen vacancies by proximity-coupling to a superconductor.

## METHODS

A series of $TiO_2$ terminated STO substrates were slowly heated up and annealed in an UHV LEED chamber at temperatures ranging from 800 °C to 900 °C followed by LEED measurements to characterize the surface structures of the STO substrates. In order to ensure the best surface quality of STO, the SR-STO substrates were annealed in an UHV chamber and then transferred directly under UHV environment to another UHV electron beam evaporator chamber for niobium film deposition at ambient temperature, where the base pressure during the film deposition was kept as low as $5\times10^{-11}$ torr. The film thickness was monitored using a quartz crystal microbalance, where the deposition rate was precalibrated by X-ray low-angle reflectivity measurements. At last, a thin aluminum film of thickness about 1 nm was subsequently deposited as a protection layer. The surface morphology of resulting Al(1 nm)/Nb(*d*)/SR-STO samples were probed using an atomic force microscope. The magnetotransport measurements were carried out using a superconducting magnet system with a variable temperature insert. For comparison, a series of control samples were fabricated with the same conditions of films deposited either on $TiO_2$-terminated STO without surface reconstruction or on $SiO_2$/Si substrates instead.

## DATA AVAILABILITY

All the supporting data are included in the main text and also in Supplementary information. The raw data and other related data for this paper can be requested from W.L.L. (wlee@phys.sinica.edu.tw).

## CODE AVAILABILITY

The input files for DFT calculations using WIEN2k are available upon request. The computer code for the calculation of Landauer conductance is written in FORTRAN90 and is also available upon request.

Received: 29 November 2019; Accepted: 2 June 2020;
Published online: 06 July 2020

## REFERENCES

1. Tarascon, J. M., Greene, L. H., Mckinnon, W. R., Hull, G. W. & Geballe, T. H. Superconductivity at 40 K in the oxygen-defect perovskites $La_{2-x}Sr_xCuO_{4-y}$. *Science* **235**, 1373–1376 (1987).
2. Cava, R. J. et al. Bulk superconductivity at 91 K in single-phase oxygen-deficient perovskite $Ba_2YCu_3O_{9-\delta}$. *Phys. Rev. Lett.* **58**, 1676–1679 (1987).
3. Liang, R., Bonn, D. A. & Hardy, W. N. Evaluation of $CuO_2$ plane hole doping in $YBa_2Cu_3O_{6+x}$ single crystals. *Phys. Rev. B* **73**, 180505 (2006).
4. Spinelli, A., Torija, M. A., Liu, C., Jan, C. & Leighton, C. Electronic transport in doped $SrTiO_3$ : conduction mechanisms and potential applications. *Phys. Rev. B* **81**, 155110 (2010).
5. Lin, X., Zhu, Z., Fauque, B. & Behnia, K. Fermi surface of the most dilute superconductor. *Phys. Rev. X* **3**, 021002 (2013).
6. Lin, C. & Demkov, A. A. Electron correlation in oxygen vacancy in $SrTiO_3$. *Phys. Rev. Lett.* **111**, 217601 (2013).
7. Lin, C. & Demkov, A. A. Consequences of oxygen-vacancy correlations at the $SrTiO_3$ interface. *Phys. Rev. Lett.* **113**, 157602 (2014).
8. Altmeyer, M. et al. Magnetism, spin texture, and in-gap states: atomic specialization at the surface of oxygen-deficient $SrTiO_3$. *Phys. Rev. Lett.* **116**, 157203 (2016).
9. Meevasana, W. et al. Creation and control of a two-dimensional electron liquid at the bare $SrTiO_3$ surface. *Nat. Mater.* **10**, 114–118 (2011).
10. Tanaka, H., Matsumoto, T., Kawai, T. & Kawai, S. Surface structure and electronic property of reduced $SrTiO_3$ (100) surface observed by scanning tunneling microscopy/spectroscopy. *Jpn. J. Appl. Phys.* **32**, 1405–1409 (1993).
11. Wang, Q. Y. et al. Interface-induced high-temperature superconductivity in single unit-cell FeSe films on $SrTiO_3$. *Chin. Phys. Lett.* **29**, 037402 (2012).
12. Lee, J. J. et al. Interfacial mode coupling as the origin of the enhancement of $T_c$ in FeSe films on $SrTiO_3$. *Nature* **515**, 245–248 (2014).
13. Ding, H. et al. High-temperature superconductivity in single-unit-cell FeSe films on Anatase $TiO_2$ (001). *Phys. Rev. Lett.* **117**, 067001 (2016).
14. He, S. et al. Phase diagram and electronic indication of high-temperature superconductivity at 65 K in single-layer FeSe films. *Nat. Mater.* **12**, 605–610 (2013).
15. Gonzalez, M. S. M. et al. In situ reduction of (100) $SrTiO_3$. *Solid State Sci.* **2**, 519–524 (2000).
16. Chen, C., Avila, J., Frantzeskakis, E., Levy, A. & Asensio, M. C. Observation of a two-dimensional liquid of Frohlich polarons at the bare $SrTiO_3$ surface. *Nat. commun.* **6**, 8585 (2015).
17. Dagdeviren, O. E. et al. Surface phase, morphology, and charge distribution transitions on vacuum and ambient annealed $SrTiO_3$ (100). *Phys., Rev. B* **93**, 195303 (2016).
18. LEEDpat, Version 4.2, utility by K.E. Hermann (FHI) and M.A. Van Hove (HKBU), Berlin/Hong Kong. http://www.fhi-berlin.mpg.de/KHsoftware/LEEDpat/index.html (2014).
19. Yoshii, K., Yamamoto, H., Saiki, K. & Koma, A. Superconductivity and electrical properties in single-crystalline ultrathin Nb films grown by molecular-beam epitaxy. *Phys. Rev. B* **52**, 13570–13575 (1995).
20. Tinkham, M. *Introduction to Superconductivity*. (Dover Publications, New York, 1996).
21. Suzuki, M. Resistance peak at the resistive transition in high-$T_c$ superconductors. *Phys. Rev. B* **50**, 6360–6365 (1994).
22. Wan, Y. M., Hebboul, S. E., Harris, D. C. & Garland, J. C. Interlayer Josephson coupling of thermally excited vortices in $Bi_2Sr_2CaCu_20_{8-y}$. *Phys. Rev. Lett.* **71**, 157–160 (1993).
23. He, Z. et al. Observation of resistivity anisotropy on oriented $YBa_2Cu_3O_7$ films. *Solid State Commun.* **76**, 671–674 (1990).
24. Buzea, C. & Yamashita, T. Structure anisotropy of high temperature superconductors: resistance peak effect. *J. Optoelectron. Adv. Mater.* **2**, 704–712 (2000).
25. Santhanam, P., Chi, C. C., Wind, S. J., Brady, M. J. & Bucchignano, J. J. Resistance anomaly near the superconducting transition temperature in short aluminum wires. *Phys. Rev. Lett.* **66**, 2254–2257 (1991).
26. Moshchalkov, V. V., Gielen, L., Neuttiens, G., Van Haesendonck, C. & Bruynseraede, Y. Intrinsic resistance fluctuations in mesoscopic superconducting wires. *Phys. Rev. B* **49**, 15412–15415 (1994).
27. Sambandamurthy, G., Engel, L. W., Johansson, A., Peled, E. & Shahar, D. Experimental evidence for a collective insulating state in two-dimensional superconductors. *Phys. Rev. Lett.* **94**, 017003 (2005).
28. Zhang, G., Zeleznik, M., Vanacken, J., May, P. W. & Moshchalkov, V. V. Metal-bosonic insulator-superconductor transition in boron-doped granular diamond. *Phys. Rev. Lett.* **110**, 077001 (2013).

29. Wang, J. et al. Interplay between superconductivity and ferromagnetism in crystalline nanowires. *Nat. Phys.* **6**, 389–394 (2010).
30. Perdew, J. P., Burke, K. & Ernzerhof, M. Generalized gradient approximation made simple. *Phys. Rev. Lett.* **77**, 3865–3868 (1996).
31. Blaha, P. et al. WIEN2k, an augmented plane wave + local orbitals program for calculating crystal properties (Karlheinz Schwarz, Techn. Universität Wien, Austria, 2018).
32. Lechermann, F., Jeschke, H. O., Kim, A. J., Backes, S. & Valentin, R. Electron dichotomy on the $SrTiO_3$ defect surface augmented by many-body effects. *Phys. Rev. B* **93**, 121103 (2016).
33. Coey, J. M. D., Venkatesan, M. & Stamenov, P. Surface magnetism of strontium titanate. *Matter* **28**, 485001 (2016).
34. Bergeret, F. S., Volkov, A. F. & Efetov, K. B. Long-range proximity effects in superconductor-ferromagnet structures. *Phys. Rev. Lett.* **86**, 4096–4099 (2001).
35. Jedema, F. J., van Wees, B. J., Hoving, B. H., Filip, A. T. & Klapwijk, T. M. Spin-accumulation-induced resistance in mesoscopic ferromagnet-superconductor junctions. *Phys. Rev. B* **60**, 16549–16552 (1999).
36. Blonder, G. E., Tinkham, M. & Klapwijk, T. M. Transition from metallic to tunneling regimes in superconducting microconstrictions: excess current, charge imbalance, and supercurrent conversion. *Phys. Rev. B* **25**, 4515–4532 (1982).

## ACKNOWLEDGEMENTS

W.L.L. acknowledges the funding supports from Academia Sinica (Thematic Research Program) and Ministry of Science and Technology of Taiwan (MOST Grant No. MOST 108-2628-M-001-007-MY3). M.D.R. and W.-C.L. were supported by the National Science Foundation under Grant No. NSF-IIS-2026702. We also thank C. Lin, W. Wu, A. Bensaoula, and Y. Matsuda for fruitful discussions.

## AUTHOR CONTRIBUTIONS

A.K.S. and U.K. grew the epitaxial films. T.C.W., B.D., S.K., and W.L.L. carried out the low temperature magneto-transport measurements and data analysis. W.H.P. and A.K.S. performed LEED measurements and analysis. M.D.R. and W.C.L. constructed theoretical model and calculation. A.K.S., W.C.L., and W.L.L. designed the experiment and wrote the paper.

## COMPETING INTERESTS

The authors declare no competing interests.

## ADDITIONAL INFORMATION

**Supplementary information** is available for this paper at https://doi.org/10.1038/s41535-020-0242-4.

**Correspondence** and requests for materials should be addressed to W.-C.L. or W.-L.L.

**Reprints and permission information** is available at http://www.nature.com/reprints

**Publisher's note** Springer Nature remains neutral with regard to jurisdictional claims in published maps and institutional affiliations.